Orbital Hall effect and orbital edge states caused by *s* electrons

Oliver Busch ●,* Ingrid Mertig ●, and Börge Göbel ●†

Institut für Physik, Martin-Luther-Universität Halle-Wittenberg, D-06099 Halle (Saale), Germany

An orbital current can be generated whenever an object has a translational degree of freedom and a rotational degree of freedom. In condensed matter physics, intra-atomic contributions to the transverse orbital transport, labeled the orbital Hall effect, rely on propagating wave packets that must consist of hybridized atomic orbitals. However, interatomic contributions have to be considered as well because they give rise to an alternative mechanism for generating orbital currents. As we show, even wave packets consisting purely of *s* electrons can transport orbital angular momentum if they move on a cycloid trajectory. We introduce the kagome lattice with a single *s* orbital per atom as the minimal model for the orbital Hall effect and observe the cycloid motion of the electrons in the surface states.

I. INTRODUCTION

The field of orbitronics is concerned with the orbital degree of freedom of electrons instead of their spin and charge [1]. Despite the fact that orbital quenching [2] leads to a suppressed orbital magnetization in most solids, orbital currents often surpass spin currents in magnitude, as the latter require considerable spin-orbit coupling to be generated. This makes orbital currents highly attractive for dissipationless orbitronic applications [3].

Charge, spin, and orbital currents can be generated by the charge [4], spin [5–8], and orbital Hall effects [9–13]: The application of an electric field leads to the generation of the different types of currents as a transverse response. While the conventional (charge) Hall effect requires a broken inversion and time-reversal symmetry, the spin and orbital Hall effects can exist even in nonmagnetic and centrosymmetric solids. The orbital Hall effect (OHE) has been predicted to exist even in systems without spin-orbit coupling, but a hybridization of different atomic orbitals has been strictly required in the models up to now [14,15].

The need for mixing of orbitals stems from the fact that earlier studies on the OHE were based on the atomic center approximation (ACA) for calculating the orbital angular momentum (OAM) [11–14]: An OAM, which is supposed to be transported as an orbital current, can only be generated at a particular lattice site. However, since the building blocks of every solid are cubic harmonic orbitals (s, p_x, p_y, p_z, d_{xy}, d_{yz}, d_{zx}, . . .), the OAM of a pure Bloch state always vanishes. The cubic harmonic orbitals need to hybridize (e.g., form the superpositions $p_x \pm \mathrm{i}\, p_y$ or $d_{yz} \pm \mathrm{i}\, d_{xz}$) in order to generate an OAM $L_z = m\hbar$. However, the ACA neglects interatomic contributions to the effect: A wave packet propagating across several lattice sites can carry an OAM irrespective of its orbital composition [16].

In this paper, we take into account the interatomic contributions to the OHE by using the modern formulation of orbital magnetization [17–23]. We show that the generation of an OHE does not require a specific orbital hybridization but can exist even for pure states. We propose a kagome lattice with only *s* orbitals as the minimal model for the generation of an orbital Hall effect. We demonstrate that the OHE arises from a cycloid motion of a wave packet that is best observed in "geometrical" [24] edge states in a finite slab geometry. These states give rise to the same orbital current irrespective of their propagation direction [red and blue in Fig. 1(a)].

II. ORBITAL CURRENTS IN MACROSCOPIC SYSTEMS

The ACA requires an often complicated hybridization of specific atomic orbitals for the generation of an OAM and an orbital magnetization [11–14]. However, these quantities may emerge irrespective of the orbital contribution if the modern formulation of orbital magnetization is considered.

In the following, we want to point out that this is not surprising. Orbital currents are not "exotic" but appear whenever objects "translate" and "circulate" simultaneously. Even for macroscopic objects in classical mechanics, orbital currents are ubiquitous, as long as there is a translational and a rotational degree of freedom. For example, the rotors of a flying airplane can be identified with an orbital current. In the local coordinate system (moving with the center of mass) there is only a finite OAM $\boldsymbol{L} = \rho \int \boldsymbol{r} \times \boldsymbol{v}\, \mathrm{d}^3 r$ since each point of the rotor follows a circular trajectory. In a global (stationary) coordinate system that lies on the path of the center of mass, the OAM is the same, but it is transported by the translational motion of the airplane. The result is an orbital current.
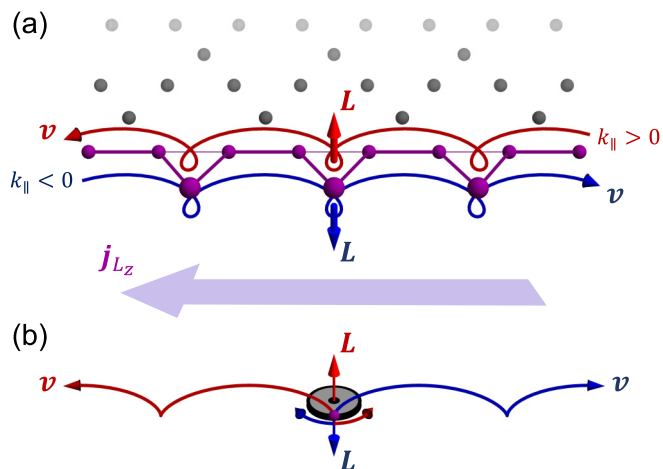
FIG. 1. Schematic representation of orbital currents. (a) Orbital current arising from edge states in a kagome lattice. Left- ($k_\parallel < 0$) and right-propagating states ($k_\parallel > 0$) carry an opposite orbital angular momentum L causing identical orbital currents j_{L_z} and a compensated charge current. (b) Orbital current of a tire rolling forward ($v > 0$) and backward ($v < 0$). Both states carry an opposite orbital angular momentum causing identical orbital currents.

As we will see later, most similar to the orbital current generated by the OHE in an s-orbital kagome model is the example of a rolling wheel (e.g., the tire of a car) [cf. Fig. 1(b)]. Without wheel slip, the friction force is strong enough to impose a constraint which couples the translational velocity (of the center of mass) v to the angular frequency $\boldsymbol{\omega}$ via the radius R: $v = R\omega$. Likewise, the angular momentum $\boldsymbol{L} \parallel \boldsymbol{\omega}$ is coupled to v via the moment of inertia I: $v = RL/I$. In particular, if v changes sign, L has to change as well. Since the orbital current $\boldsymbol{j}_L$ is proportional to $\boldsymbol{v} \times \boldsymbol{L}$, it is identical for forward and backward motion even though $\boldsymbol{L}$ reverses.

Consequently, if one considers two wheels moving in opposite directions [red and blue in Fig. 1(b)], the total OAM $\boldsymbol{L}$ is compensated. but a net orbital current $\boldsymbol{j}_L$ arises. The trajectory of each point on the wheels is a cycloid in the global coordinate systems and a circle in the local coordinate system (origin is in the center of mass). As we demonstrate next, we observe an analogous scenario for $\boldsymbol{j}_L$ and the same type of trajectory for a wave packet propagating at the edge of a kagome lattice [cf. Fig. 1(a)]. Here, the OAM $\boldsymbol{L}$ is coupled to the group velocity $\boldsymbol{v} = \nabla_{\boldsymbol{k}}\varepsilon/\hbar$.

III. ORBITAL HALL EFFECT

In the existing literature, the hybridization of different cubic orbitals was claimed to be the origin of the OHE [11,13,14]. It was argued that they need to form the spherical harmonic orbitals with a net magnetic quantum number m that gives rise to a finite OAM [14,15]. As discussed in the Introduction, this is indeed the only possibility to generate an OHE when using the ACA. For example, a spherical atomic orbital with angular momentum quantum number $l = 1$ and magnetic quantum number $m = +1$ is formed by the superposition of the cubic orbitals p_x and p_y as $|l = 1, m = 1\rangle = (|p_x\rangle - \mathrm{i}|p_y\rangle)/\sqrt{2}$ and gives rise to $L_z = m\hbar = +\hbar$.

In order to be able to account for the transported OAM via a cycloid trajectory, it is not sufficient to use the ACA for calculating the OHE. Instead, we take into account intersite contributions via the modern formulation of orbital magnetization [17–20] and use it to calculate the OHE regardless of the orbital composition. The calculation is not based on the on-site OAM operator that accounts for the hybridization of the cubic atomic orbitals, but it is calculated from the eigenvectors $|\nu\boldsymbol{k}\rangle \equiv |\varphi_\nu(\boldsymbol{k})\rangle$ and the eigenenergies $\varepsilon_{\nu\boldsymbol{k}} \equiv \varepsilon_\nu(\boldsymbol{k})$ of the tight-binding Hamiltonian that are $\boldsymbol{k}$ dependent.

The orbital Hall conductivity (OHC) $\sigma_{xy}^{L_z}$ quantifies the OHE by relating the generated orbital current to the applied electric field $j_x^{L_z} = \sigma_{xy}^{L_z}E_y$. The OHC of a two-dimensional system at zero temperature located in the xy plane, as considered in this paper, can be computed as [13,14,21]

$$\sigma_{xy}^{L_z}(E_{\mathrm{F}}) = \frac{e}{\hbar}\sum_\nu \frac{1}{(2\pi)^2}\int_{\varepsilon_{\nu k} \leqslant E_{\mathrm{F}}} \Omega_{\nu,xy}^{L_z}(\boldsymbol{k})\,\mathrm{d}^2k \qquad (1)$$

for a specific Fermi level E_{F}. By analogy with the spin Hall conductivity, the OHC is given as the Brillouin zone integral of a "mixed Berry curvature" that is labeled the "orbital Berry curvature" [21]

$$\Omega_{\nu,xy}^{L_z}(\boldsymbol{k}) = -2\hbar^2\,\mathrm{Im}\sum_{\mu\neq\nu}\frac{\langle\nu\boldsymbol{k}|\Lambda_x^z|\mu\boldsymbol{k}\rangle\langle\mu\boldsymbol{k}|v_y|\nu\boldsymbol{k}\rangle}{(\varepsilon_{\nu\boldsymbol{k}} - \varepsilon_{\mu\boldsymbol{k}})^2}. \qquad (2)$$

Herein, $v_i = \frac{1}{\hbar}\frac{\partial H}{\partial k_i}$ is the velocity operator that is calculated from the Hamiltonian H. The orbital current operator is given by $\Lambda_x^z \equiv \frac{1}{2}\{v_x, L^z\}$ and can be evaluated according to the modern formulation of orbital magnetization via

$$\langle\nu\boldsymbol{k}|\Lambda_x^z|\mu\boldsymbol{k}\rangle = \frac{1}{2}\sum_\alpha [\langle\nu\boldsymbol{k}|v_x|\alpha\boldsymbol{k}\rangle\langle\alpha\boldsymbol{k}|L_z|\mu\boldsymbol{k}\rangle$$
$$+ \langle\nu\boldsymbol{k}|L_z|\alpha\boldsymbol{k}\rangle\langle\alpha\boldsymbol{k}|v_x|\mu\boldsymbol{k}\rangle].$$

The matrix elements of the OAM comprise both diagonal elements and off-diagonal elements

$$\langle\nu\boldsymbol{k}|L_z|\alpha\boldsymbol{k}\rangle = -\mathrm{i}\frac{e\hbar^2}{4g_L\mu_{\mathrm{B}}}\sum_{\beta\neq\nu,\alpha}\left(\frac{1}{\varepsilon_{\beta\boldsymbol{k}} - \varepsilon_{\nu\boldsymbol{k}}} + \frac{1}{\varepsilon_{\beta\boldsymbol{k}} - \varepsilon_{\alpha\boldsymbol{k}}}\right)$$
$$\times \left(\langle\nu\boldsymbol{k}|v_x|\beta\boldsymbol{k}\rangle\langle\beta\boldsymbol{k}|v_y|\alpha\boldsymbol{k}\rangle - \langle\nu\boldsymbol{k}|v_y|\beta\boldsymbol{k}\rangle\langle\beta\boldsymbol{k}|v_x|\alpha\boldsymbol{k}\rangle\right), \qquad (3)$$

which is different compared with the ACA, where $\langle\nu\boldsymbol{k}|L_z|\alpha\boldsymbol{k}\rangle$ are constant matrix elements that mix different orbitals that are located at the same lattice site. The above equations were derived by Pezo *et al.* [21,23] based on the modern formulation of the orbital magnetization in the language of wave packet dynamics [18]. The full derivation can be found in the main text and Supplemental Material of Ref. [21], but we have corrected a mistake in Eq. (3) [25]. Note that in a finite sample the derivation differs slightly: As presented in Ref. [26], the velocity matrix elements can be calculated from the commutator between the position and the Hamilton operator.
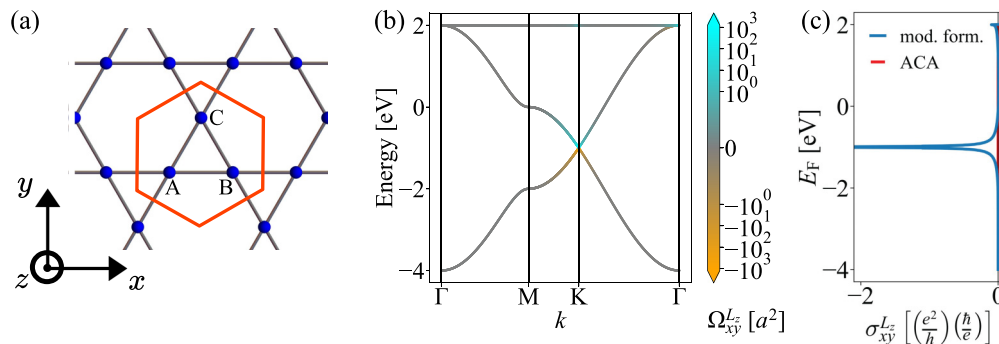
FIG. 2. Orbital Hall effect in an *s*-orbital kagome lattice. (a) Kagome lattice with three basis atoms (atoms A, B, and C) per unit cell (red hexagon). (b) Band structure of the bulk system, where the color of the bands indicates the orbital Berry curvature $\Omega_{xy}^{L_z}$ using the modern formulation (mod. form.; cyan, positive; orange, negative). (c) Orbital Hall conductivity as a function of the Fermi level E_F. Blue and red (zero) correspond to the modern formulation and ACA, respectively.

IV. MINIMAL MODEL: KAGOME LATTICE WITH *s* ORBITALS

As a minimal model that illustrates the crucial importance of using the modern formulations for computing the OHE, we have chosen a planar kagome lattice. This two-dimensional hexagonal lattice with a three-atom unit cell [cf. Fig. 2(a)] can be found in several materials including the ferromagnetic "kagome magnets" Fe_3Sn_2 [27,28] or $Co_3Sn_2S_2$ [29,30] and the famous chiral antiferromagnets Mn_3X ($X =$ Ir, Rh, Pt, Ge, Sn, and Ga) [31–34].

Since the main goal of this paper is to show that considering the ACA is not sufficient to calculate the OHE, we completely avoid any hybridization of orbitals by using one *s* orbital per lattice site. Note that this orbital does not exhibit an on-site OAM (quantum number $l = 0$ and so $m = 0$). This means that only the modern formulation of the orbital magnetization contributes to the OHE via interatomic contributions. The ACA would always return a vanishing OHE, which is why this formalism is inappropriate to quantify the effect.

Since *s* orbitals do not exhibit spin-orbit coupling, our minimal model Hamiltonian includes only hopping terms $H = t \sum_{\langle i,j \rangle} c_i^\dagger c_j$ with the creation operator $c_i^\dagger$ and the annihilation operator c_i of an electron at atom *i*. For simplicity, we consider only nearest-neighbor hopping and use $t = -1$ eV. In matrix form, the Hamiltonian reads

$$H = \begin{pmatrix} 0 & h_{AB} & h_{AC} \\ h_{BA} & 0 & h_{BC} \\ h_{CA} & h_{CB} & 0 \end{pmatrix} \quad (4)$$

with **k**-dependent entries $h_{AB} = h_{BA} = 2t \cos(k_x a)$, $h_{AC} = h_{CA} = 2t \cos(\frac{1}{2}k_x a + \frac{\sqrt{3}}{2}k_y a)$, and $h_{BC} = h_{CB} = 2t \cos(-\frac{1}{2}k_x a + \frac{\sqrt{3}}{2}k_y a)$ and the lattice constant *a*. We consider spin; so the matrix becomes 6×6. The electronic band structure $\varepsilon_\nu(\mathbf{k})$ [cf. Fig. 2(b)] exhibits Dirac points similar to the ones found in honeycomb lattices, such as graphene [cf. Figs. 5(a) and 5(b) in Appendix A]. Additionally, a flat band arises from the three-atom basis that allows for closed loops and is not present in honeycomb lattices. All bands are spin degenerate due to inversion symmetry $\mathcal{I}$ and time-reversal symmetry $\mathcal{T}$ of the system in the absence of spin-orbit coupling.

As expected, the OHC vanishes in ACA because *s* electrons do not carry an on-site OAM. However, in the modern formulation, the OHC is finite and depends on the location of the Fermi level [cf. Fig. 2(c)]. The curve is almost constant within the bands but changes strongly at the band edges near the Dirac point and close to the flat band. For an occupation of two electrons per unit cell, the Fermi level is located at the Dirac point where the OHC is diverging.

Still, the effect cannot be attributed to the Dirac points alone, since a honeycomb lattice returns the same band structure (minus the flat band) but exhibits a vanishing OHC even in the modern formulation [cf. Fig. 5(c) in Appendix A]. The reason why two almost identical band structures result in drastically different orbital Hall effects is that the OHC [Eq. (1)] is determined by the eigenvectors as well.

The on-site (diagonal) elements of the OAM L_z, calculated by Eq. (3), vanish identically for all bands in the whole Brillouin zone (not shown here). However, the off-diagonal elements $\langle \nu\mathbf{k}|L_z|\alpha\mathbf{k}\rangle$ are finite in the kagome system, and they enter the matrix elements of the orbital current operator Λ_x^z and result in a finite orbital Berry curvature, which is encoded as a color code (cyan, positive; orange, negative) in the electronic structure [cf. Fig. 2(b)]. This means that no net OAM can be measured, even though the OHC is finite, and that the transported OAM is not generated at an individual lattice site but intersite contributions (off-diagonal elements) arise which correspond to a Bloch state that is spread out over all atoms in the unit cell. Thus the situation is comparable to the spin Hall effect, which can be finite despite a compensated spin magnetization *S*.

Unfortunately, a trajectory of electron wave packets cannot be analyzed for the bulk system, as the tight-binding formalism only allows us to access the probability density. However, investigating a slab geometry (nanoribbon) allows for a deeper insight into the origin of the orbital Hall effect.

V. EDGE STATES GENERATING CYCLOID TRAJECTORIES

A slab of the considered kagome system is only periodic along one direction giving rise to a single wave vector $k_\parallel$. Edges are introduced along the perpendicular direction. This
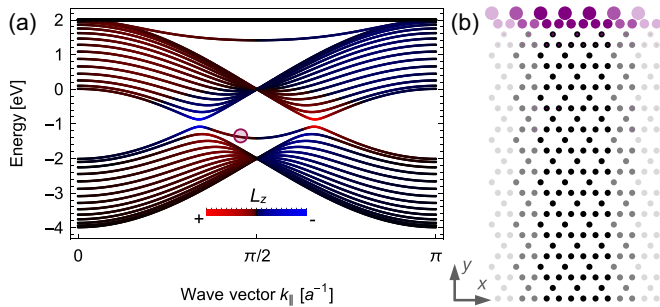
FIG. 3. Edge states in an asymmetric kagome-lattice slab that is periodic along the x direction. (a) Surface band structure along $k_{\parallel}$. The color indicates positive (red) and negative (blue) values of L_z. (b) Considered slab with probability density (area of purple circles) of the surface state indicated in (a) for $k_{\parallel} = 0.95^{\pi}/_{2a}$.

gives rise to a large unit cell and many bands in the slab band structure. The vast majority of these bands represent a projection of the bulk band structure, which is why signatures such as the Dirac points and the flat band appear in the slab band structure as well. Note that small supercell gaps occur due to the finite width of the system and that they converge to zero in the limit of an infinitely wide nanoribbon. However, caused by the edges, we observe features that were absent in the bulk band structure: the so-called surface states.

These states depend strongly on the specific shape of the edge: Most famously, a zigzag edge in a honeycomb lattice, such as graphene, exhibits an edge state, while an armchair edge does not [35–37]. For the kagome lattice, we observe several edge states for multiple edge geometries and want to focus on the geometry presented in Fig. 3, which has one "straight" edge and one "triangular" edge [cf. bottom and top edges of the sketch in Fig. 3(b)].

An edge state occurs close to the flat band, and another occurs between the two Dirac points [cf. Fig. 3(a)]. Their Chern numbers C are zero due to the time-reversal symmetry of the system. In Ref. [24] they have been labeled "geometrical edge states." In contrast to the edge state in zigzag graphene, these states have a finite group velocity $v_\nu(k_{\parallel}) = \frac{1}{\hbar}\frac{\partial \varepsilon_\nu(k_{\parallel})}{\partial k_{\parallel}} \neq 0$ allowing electron wave packets to propagate along the edges.

The edge states are symmetric with respect to $k_{\parallel}$; for each right-propagating state at $+k_0$ there is a left-propagating state at $-k_0$. Due to the vanishing Chern numbers, the edges do not cause a quantum Hall effect. The Z_2 invariant and the spin Hall effect vanish as well because all the bands are spin degenerate due to the absence of spin-orbit coupling.

However, the OAM L_z is nonzero and has an opposite sign comparing states at $+k_0$ and $-k_0$. Note that L_z has been zero in the bulk because due to the periodic repetition of the three-atom unit cell, each upward-facing triangle automatically forms a neighboring downward-facing triangle with the same occupation. Therefore each circular orbit in the bulk automatically generates an orbit with opposite circumferential direction resulting in a compensated L_z. At the triangular edge, this balance of upward- and downward-facing triangles is impaired, and so a finite L_z can be generated [color in Fig. 3(a)].

In Fig. 3(b) we show the probability density of electrons for the surface state between the Dirac points at $k_{\parallel} = 0.95\frac{\pi}{2a}$.

Typical for an edge state, the probability density is largest for lattice sites close to the edge and decays exponentially going further into the bulk. In particular, the probability density is largest for the corners of the triangles at the very edge. Even though we can still only calculate the probability density and no currents, this distribution of electrons is in agreement with a cycloid trajectory as presented in Fig. 1(a). If a wave packet consists of $+k_0$ and $-k_0$ states, the scenario is in analogy with the forward and backward rolling wheel [cf. Fig. 1(b)], as discussed in the beginning of this paper: Edge states propagating along the right carry an opposite OAM compared with edge states propagating along the left, resulting in the same orbital current.

Our understanding of the behavior at the edge can be further condensed by considering a quasi-one-dimensional chain resembling the triangles at the very edges. Such a simplistic three-atom model allows us to calculate similar $k_{\parallel}$-resolved OAM and orbital currents as long as the chain does not have a glide-mirror symmetry with a symmetry axis along the periodic direction. In Appendix B, we demonstrate that the asymmetric chain, as we find at the edge of the considered kagome lattice, leads to an orbital current [Figs. 6(b) and 6(c)]. The cycloid trajectory with a curvature of constant sign can be understood as a superposition of a translation and a rotation as discussed before [cf. Fig. 1(a)]. On the other hand, a symmetric zigzag chain cannot exhibit an orbital current since the probability density corresponds to a sinelike trajectory with alternating curvatures that compensate each other [Figs. 6(e) and 6(g)] resulting in $L = 0$. Note that in a honeycomb lattice, a symmetric zigzag-shaped edge leads to a dispersionless surface state [38] and therefore no orbital current can be generated. This also agrees with the finding that the OHE vanishes for a honeycomb lattice, such as graphene, even in the modern theory.

So far, we have only taken into account s orbitals (which are equivalent to p_z orbitals for two-dimensional systems located in the xy plane). Taking into account all three p orbitals causes hybridization of p_x and p_y, which results in a finite OHE even within the ACA approach, similar to the findings in Ref. [14]. OAM-polarized edge states arise in this case as well, as shown for a related material, PtS$_2$, in Ref. [39]. If spin-orbit coupling is considered, one observes a partial conversion of the OHE into the spin Hall effect as shown by Go *et al.* using the ACA [14]. Spin-orbit coupling lifts the spin degeneracy and the edge state splits up as shown by Sun *et al.* [40].

A categorization of the quantum Hall effect, the quantum spin Hall effect, and the edge signature of the orbital Hall effect can be found in Fig. 4. Even though their origins are fundamentally different, the spin Hall effect (SHE) and OHE exhibit similar transport of (spin or orbital) angular momentum not only in the bulk but also along the edge. The SHE caused by an edge state is quantized due to the complete spin polarization of the surface states. This is not the case for the OHE because L is not quantized. In contrast to the quantized versions of the charge and SHE, the orbital edge current is not protected. In the considered kagome system, the edge contribution to the OHE appears in its pure form and is carried by a geometrical edge state that does not bridge the gap between two bulk bands [cf. Fig. 4(c)]. However,
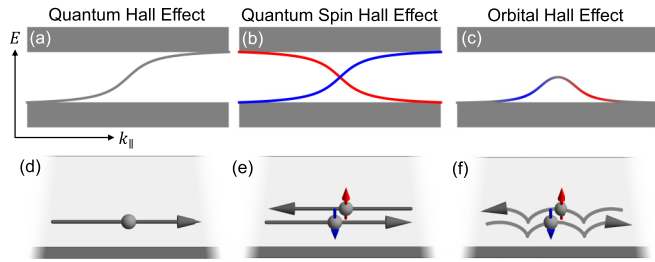
FIG. 4. Comparison of edge states and corresponding edge transport. (a) Schematic band structure of a slab giving rise to the quantum Hall effect. The bulk conduction and valence bands (gray rectangles) are connected by a chiral edge state that is not spin polarized (gray). (b) Quantum spin Hall effect. The two edge states are spin polarized (red, up; blue, down). (c) Orbital Hall effect. The geometric edge state does not bridge the gap and is partially polarized with respect to the orbital angular momentum (red, positive; blue, negative). (d)–(f) Corresponding edge currents in real space. The colored arrows in (e) correspond to the spin, and those in (f) correspond to the orbital angular momentum.

especially when spin-orbit coupling is considered, the SHE and OHE may arise at the same time, and the edge states can disperse differently. The gap may be bridged, and the topological invariants C and Z_2 may become nonzero integers giving rise to a quantum Hall effect and quantum SHE that may be superimposed with the edge contribution to the OHE.

VI. CONCLUSION

In conclusion, we used the method derived in Ref. [21] to account for intersite contributions to the OHE. While it has been known that these contributions can drastically differ from the ACA, our study demonstrates the emergence of a net OHE in a kagome lattice composed solely of s orbitals in which the OHE based on the ACA is strictly zero. Importantly, we find that the OHE is a more prevalent phenomenon compared with the spin Hall effect and can appear without a specific orbital composition. The emergence of orbital currents occurs more easily and is more omnipresent than anticipated by the ACA. Furthermore, we identify edge contributions to the OHE. The existence of edge states in this lattice gives rise to wave packets following a cycloid trajectory, akin to the trajectory of a particle on a rolling wheel. These observations highlight the significance of the OHE in various materials and its relevance for dissipationless orbitronic applications.

The magnitude of the calculated effect is considerable. At 1/3 filling, the OHC is diverging in an ideal sample. In a realistic material, in which the Dirac point opens slightly, we expect values up to several $\frac{e}{2\pi}$. Therefore they are of the same order of magnitude as typical spin Hall conductivities and the orbital Hall conductivities that have been calculated before using the ACA for other materials such as $4d$ and $5d$ transition metals [12,13] and later $3d$ materials [41] and Pt [14]. Recently, the OHE has been observed experimentally in Ti using the magneto-optical Kerr effect, in which intersite contributions are already included [42]. Furthermore, orbital

currents have recently been detected on ultrafast time scales by terahertz emission spectroscopy measurements [43].

Moreover, we note that our findings bear relevance to the valley Hall effect [44,45], which has garnered significant attention in graphene research. In the context of the kagome lattice, the presence of distinct Dirac points at K and K', which differ in a physical quantity, gives rise to a Hall effect in that quantity. This unique characteristic is exemplified in this paper, where the opposite orbital angular momentum associated with k and $-k$ states [extrema of L_z at the Dirac points in Fig. 3(a)] leads to the observed OHE.

Importantly, the OHE is not limited to a specific material. Rather, it is expected to manifest in kagome materials, as well as materials that allow for loops in the unit cell. This generality expands the potential avenues for exploring and harnessing the OHE in diverse systems. We have carried out additional calculations and find that it is present also in a square-octagon lattice (cf. Fig. 5 in Appendix A) which has four basis atoms forming a square in the unit cell.

APPENDIX A: COMPARISON OF DIFFERENT TWO-DIMENSIONAL MODEL LATTICES

In this Appendix, we compare the orbital Hall conductivity (OHC) $\sigma_{xy}^{L_z}$ in four different model lattices. The results are presented in Fig. 5. In the atomic center approximation (ACA), the OHC vanishes in all cases because we consider only s electrons that are characterized by the orbital angular momentum quantum number $l = 0$. For simplicity, only nearest-neighbor hoppings with amplitudes $t = -1$ eV are considered. In the following, we want to discuss the orbital Berry curvature and the OHC in the modern formulation.

Figure 5(a) shows a honeycomb lattice such as that in graphene. The band structure in Fig. 5(b) shows the typical features such as the Dirac cone at K. The orbital Berry curvature based on the modern formulation [Eq. (2)] is zero everywhere, which is the reason why the OHC is zero for every energy [Fig. 5(c)]. The second row [Figs. 5(d)–5(f)] shows the same results for the kagome lattice. This time the orbital Berry curvature is nonzero as discussed in the main text. This leads to an energy-dependent OHC that exhibits a sharp peak close to the energy of the Dirac point.

The third [Figs. 5(g)–5(i)] and fourth rows [Figs. 5(j)–5(l)] show the results for a square lattice and a square-octagon lattice, respectively. The results are similar to the comparison of the honeycomb and kagome lattices: Like the honeycomb lattice, the square lattice [Fig. 5(g)] has no closed loops in the unit cell. The orbital Berry curvature [Fig. 5(h)] vanishes everywhere, and the OHC [Fig. 5(i)] is zero for every energy. However, the square-octagon lattice [Fig. 5(j)] has four atoms
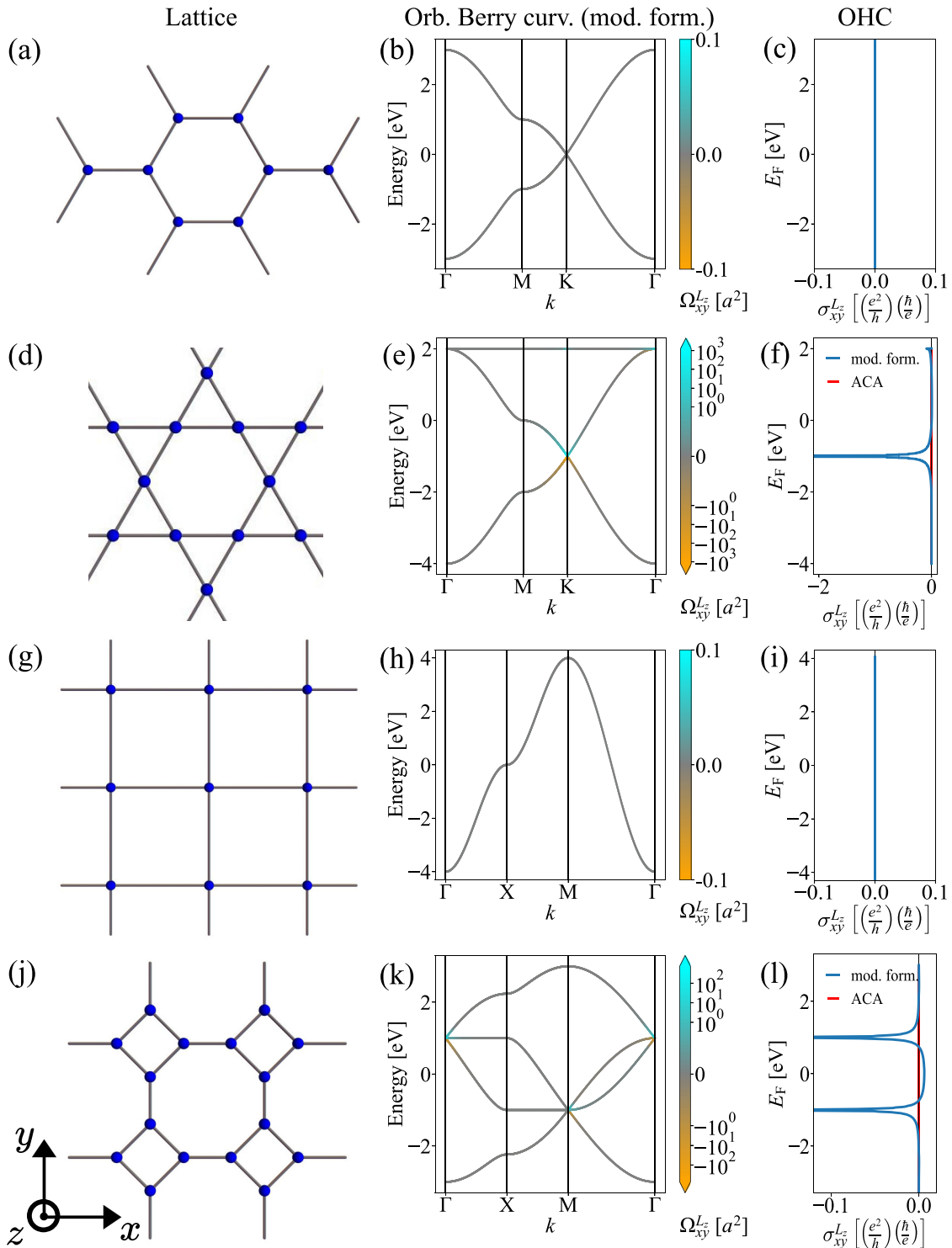
FIG. 5. Comparison of different two-dimensional model lattices with s orbitals located at the atomic sites (from the top row to the bottom row: honeycomb, kagome, square, and square-octagon lattices). (a) Honeycomb lattice as found in graphene. (b) Electronic structure with (vanishing) orbital Berry curvature (orb. Berry curv.) $\Omega_{xy}^{L_z}$ using the modern formulation (cyan, positive; orange, negative; gray, zero). (c) OHC $\sigma_{xy}^{L_z}$ as a function of the Fermi energy E_F; the OHC vanishes for both methods: ACA and modern theory. (d)–(f) Analog results for the kagome lattice, which exhibits a finite OHE, however, only if the modern formulation is used [cf. Fig. 2]. (g)–(i) Analog results for a square lattice, which does not exhibit an OHE. (j)–(l) Analog results for the square-octagon lattice, which allows for a finite OHE using the modern formulation.
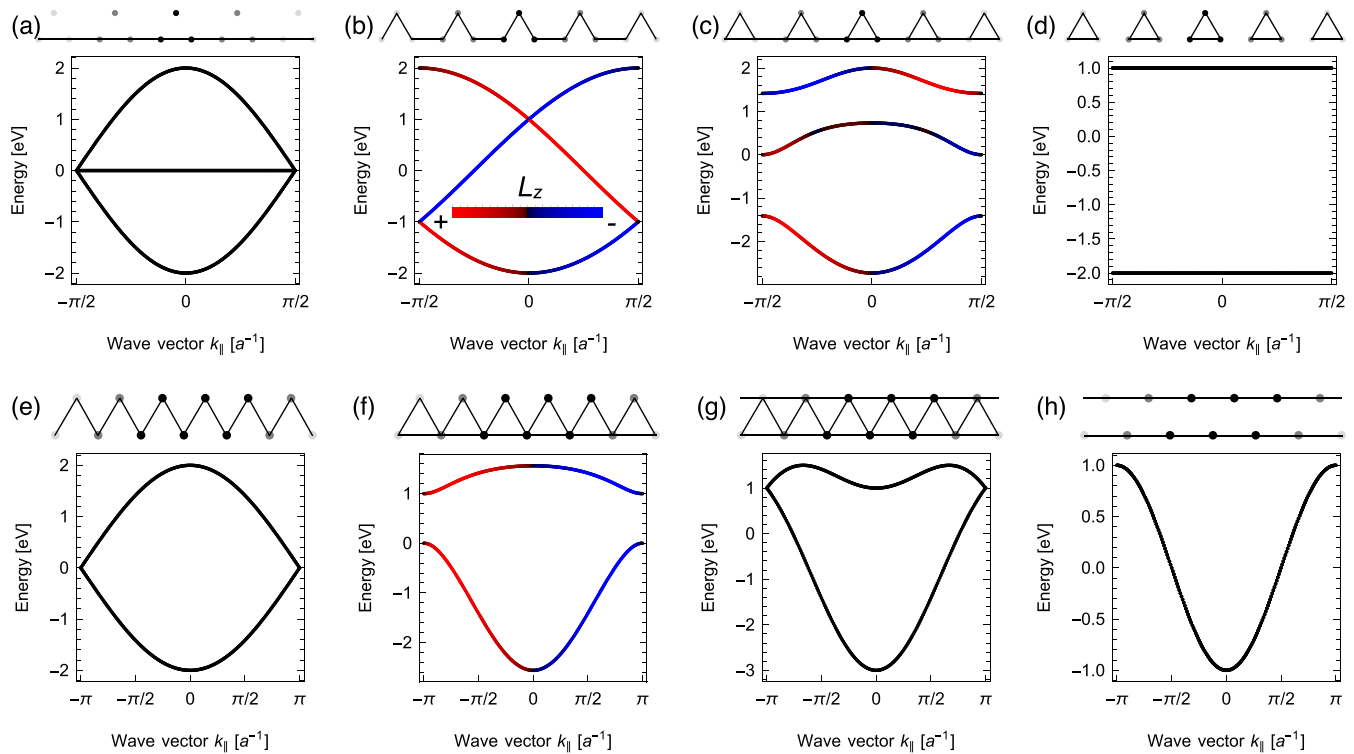
FIG. 6. Band structure and orbital angular momentum L_z (color is the same as in Fig. 3) for various quasi-one-dimensional chains. (a)–(d) Quasi-one-dimensional chain resembling the edge of the kagome slab with three atoms in the unit cell. (a) No L_z is generated (gray) when the edge is a straight line. (b) L_z is finite (red and blue) and antisymmetric with respect to $k_\parallel$ once the additional atom is taken into account and the edge becomes asymmetric. (c) The same is true if all nearest-neighbor hoppings are considered. (d) Closed, unconnected loops are not sufficient to generate L_z. Since the individual triangles are not connected by hopping paths, the bands have no dispersion. (e)–(h) Simplified versions of the systems, consisting of a zigzag chain with two atoms in the unit cell. (e) A symmetric zigzag edge does not generate a finite L_z. (f) Once we artificially make the edge asymmetric by considering additional hoppings, L_z is generated. (g) and (h) In these scenarios the edge becomes symmetric again, giving rise to $L_z = 0$.

in the unit cell that allow for closed loops of the electron wave packets. The orbital Berry curvature according to the modern formulation [Fig. 5(k)] is nonzero, and the corresponding OHC [Fig. 5(l)] exhibits sharp peaks at the two Dirac points.

APPENDIX B: ORBITAL CURRENTS IN VARIOUS QUASI-ONE-DIMENSIONAL CHAINS

In the main text, we have discussed that an orbital current can arise when an object "translates" and "circulates" at the same time. At the triangular edge of the kagome nanoribbon, such a trajectory is present, which can give rise to a contribution to the OHC. In Fig. 6 we compare different quasi-one-dimensional chains, corresponding to possible edges of nanoribbons, and calculate their band structure and k-resolved orbital angular momentum. The graphs above the band structures resemble the considered system. The circles are the lattice sites, and the lines are the considered hoppings with strength $t_i = -1$ eV. All systems are periodic along the chain direction.

In Figs. 6(a)–6(d) the chain is like the edge of the kagome nanoribbon and consists of three atoms. However, we manipulate the hopping to figure out in which scenario translation (characterized by dispersion in the band structure, $v = \frac{1}{\hbar}\frac{\partial H}{\partial k_\parallel}$) and rotation (characterized by an orbital angular momentum

L_z) are present. In that case, an orbital current arises which contributes to the OHC.

In Fig. 6(a) an electron can propagate along the edge, so the band structure shows dispersion. However, since there are no closed loops of the hopping paths, the orbital angular momentum vanishes for every k point. For this reason, no orbital current arises. Note that the additional "unconnected" atom results in a dispersionless band because the hopping to this atom is disregarded here. In Figs. 6(b) and 6(c) the band structure exhibits dispersion, and the orbital angular momentum is nonzero for most k points, which is why an orbital current can arise in that case. Both scenarios resemble the edge of the kagome nanoribbon from the main text quite accurately and explain how the L_z and orbital Hall conductivity arise at the edge of a kagome slab. The only difference between the two chains is that in Fig. 6(c) closed loops are present, while in Fig. 6(b) this is not the case. Still, since the edge is asymmetric, the corresponding cycloid trajectory transports an orbital angular momentum, as explained in the main text. In Fig. 6(d), the individual triangular unit cells are not connected by hoppings. The band structure exhibits no dispersion, and no orbital currents can arise.

In the second row [Figs. 6(e)–6(h)], we present results for simplified systems. These systems, consisting of a zigzag chain with two atoms in the unit cell, allow for the

generation of orbital currents as well if the hoppings are chosen as in Fig. 6(f). The top and the bottom edges must be inequivalent; otherwise the orbital angular momentum is compensated due to the glide-mirror symmetry that is present in Fig. 6(g). The same is true for the systems presented in Figs. 6(e) and 6(h), which is why the band structure shows dispersion but no k-resolved orbital angular momentum is generated.

[1] D. Go, D. Jo, H.-W. Lee, M. Kläui, and Y. Mokrousov, Orbitronics: Orbital currents in solids, Europhys. Lett. **135**, 37001 (2021).

[2] C. Kittel, Surface and interface physics, in *Introduction to Solid State Physics* (Wiley, New York, 2004), Chap. 17, pp. 487–514.

[3] Y. Cao, G. Xing, H. Lin, N. Zhang, H. Zheng, and K. Wang, Prospect of spin-orbitronic devices and their applications, iScience **23**, 101614 (2020).

[4] N. Nagaosa, J. Sinova, S. Onoda, A. H. MacDonald, and N. P. Ong, Anomalous Hall effect, Rev. Mod. Phys. **82**, 1539 (2010).

[5] M. I. D'yakonov and V. I. Perel, Current-induced spin orientation of electrons in semiconductors, Phys. Lett. A **35**, 459 (1971).

[6] J. E. Hirsch, Spin Hall effect, Phys. Rev. Lett. **83**, 1834 (1999).

[7] Y. K. Kato, R. C. Myers, A. C. Gossard, and D. D. Awschalom, Observation of the spin Hall effect in semiconductors, Science **306**, 1910 (2004).

[8] J. Sinova, S. O. Valenzuela, J. Wunderlich, C. H. Back, and T. Jungwirth, Spin Hall effects, Rev. Mod. Phys. **87**, 1213 (2015).

[9] S. Zhang and Z. Yang, Intrinsic spin and orbital angular momentum Hall effect, Phys. Rev. Lett. **94**, 066602 (2005).

[10] B. A. Bernevig, T. L. Hughes, and S.-C. Zhang, Orbitronics: The intrinsic orbital current in p-doped silicon, Phys. Rev. Lett. **95**, 066601 (2005).

[11] H. Kontani, T. Tanaka, D. S. Hirashima, K. Yamada, and J. Inoue, Giant intrinsic spin and orbital Hall effects in Sr$_2M$O$_4$ (M = Ru, Rh, Mo), Phys. Rev. Lett. **100**, 096601 (2008).

[12] T. Tanaka, H. Kontani, M. Naito, T. Naito, D. S. Hirashima, K. Yamada, and J. Inoue, Intrinsic spin Hall effect and orbital Hall effect in $4d$ and $5d$ transition metals, Phys. Rev. B **77**, 165117 (2008).

[13] H. Kontani, T. Tanaka, D. S. Hirashima, K. Yamada, and J. Inoue, Giant orbital Hall effect in transition metals: Origin of large spin and anomalous Hall effects, Phys. Rev. Lett. **102**, 016601 (2009).

[14] D. Go, D. Jo, C. Kim, and H.-W. Lee, Intrinsic spin and orbital Hall effects from orbital texture, Phys. Rev. Lett. **121**, 086602 (2018).

[15] D. Go and H.-W. Lee, Orbital torque: Torque generation by orbital current injection, Phys. Rev. Res. **2**, 013177 (2020).

[16] M.-C. Chang and Q. Niu, Berry phase, hyperorbits, and the Hofstadter spectrum: Semiclassical dynamics in magnetic Bloch bands, Phys. Rev. B **53**, 7010 (1996).

[17] T. Thonhauser, D. Ceresoli, D. Vanderbilt, and R. Resta, Orbital magnetization in periodic insulators, Phys. Rev. Lett. **95**, 137205 (2005).

[18] D. Xiao, J. Shi, and Q. Niu, Berry phase correction to electron density of states in solids, Phys. Rev. Lett. **95**, 137204 (2005).

[19] J. Shi, G. Vignale, D. Xiao, and Q. Niu, Quantum theory of orbital magnetization and its generalization to interacting systems, Phys. Rev. Lett. **99**, 197202 (2007).

[20] T. Yoda, T. Yokoyama, and S. Murakami, Orbital Edelstein effect as a condensed-matter analog of solenoids, Nano Lett. **18**, 916 (2018).

[21] A. Pezo, D. Garcia Ovalle, and A. Manchon, Orbital Hall effect in crystals: Interatomic versus intra-atomic contributions, Phys. Rev. B **106**, 104414 (2022).

[22] T. P. Cysne, S. Bhowal, G. Vignale, and T. G. Rappoport, Orbital Hall effect in bilayer transition metal dichalcogenides: From the intra-atomic approximation to the Bloch states orbital magnetic moment approach, Phys. Rev. B **105**, 195421 (2022).

[23] A. Pezo, D. G. Ovalle, and A. Manchon, Orbital Hall physics in two-dimensional Dirac materials, Phys. Rev. B **108**, 075427 (2023).

[24] B.-J. Yang and N. Nagaosa, Emergent topological phenomena in thin films of pyrochlore iridates, Phys. Rev. Lett. **112**, 246402 (2014).

[25] We replaced "Im" (determining the imaginary part of the following expression) by the negative of the imaginary unit "$-i$".

[26] D. Go, J.-P. Hanke, P. M. Buhl, F. Freimuth, G. Bihlmayer, H.-W. Lee, Y. Mokrousov, and S. Blügel, Toward surface orbitronics: giant orbital magnetism from the orbital Rashba effect at the surface of sp-metals, Sci. Rep. **7**, 46742 (2017).

[27] J.-X. Yin, S. S. Zhang, H. Li, K. Jiang, G. Chang, B. Zhang, B. Lian, C. Xiang, I. Belopolski, H. Zheng, T. A. Cochran, S.-Y. Xu, G. Bian, K. Liu, T.-R. Chang, H. Lin, Z.-Y. Lu, Z. Wang, S. Jia, W. Wang *et al.*, Giant and anisotropic many-body spin–orbit tunability in a strongly correlated kagome magnet, Nature (London) **562**, 91 (2018).

[28] D. Khadka, T. R. Thapaliya, S. Hurtado Parra, J. Wen, R. Need, J. M. Kikkawa, and S. X. Huang, Anomalous Hall and Nernst effects in epitaxial films of topological kagome magnet Fe$_3$Sn$_2$, Phys. Rev. Mater. **4**, 084203 (2020).

[29] E. Liu, Y. Sun, N. Kumar, L. Muechler, A. Sun, L. Jiao, S.-Y. Yang, D. Liu, A. Liang, Q. Xu, J. Kroder, V. Süß, H. Borrmann, C. Shekhar, Z. Wang, W. Wang, W. Schnelle, S. Wirth, Y. Chen *et al.*, Giant anomalous Hall effect in a ferromagnetic kagome-lattice semimetal, Nat. Phys. **14**, 1125 (2018).

[30] O. V. Yazyev, An upside-down magnet, Nat. Phys. **15**, 424 (2019).

[31] H. Chen, Q. Niu, and A. H. MacDonald, Anomalous Hall effect arising from noncollinear antiferromagnetism, Phys. Rev. Lett. **112**, 017205 (2014).

[32] S. Nakatsuji, N. Kiyohara, and T. Higo, Large anomalous Hall effect in a non-collinear antiferromagnet at room temperature, Nature (London) **527**, 212 (2015).

[33] A. K. Nayak, J. E. Fischer, Y. Sun, B. Yan, J. Karel, A. C. Komarek, C. Shekhar, N. Kumar, W. Schnelle, J. Kübler, C. Felser, and S. S. P. Parkin, Large anomalous Hall effect driven by a nonvanishing Berry curvature in the noncolinear antiferromagnet Mn$_3$Ge, Sci. Adv. **2**, e1501870 (2016).

[34] Y. Zhang, Y. Sun, H. Yang, J. Železný, S. P. P. Parkin, C. Felser, and B. Yan, Strong anisotropic anomalous Hall effect and spin Hall effect in the chiral antiferromagnetic compounds Mn$_3X$

($X =$ Ge, Sn, Ga, Ir, Rh, and Pt), Phys. Rev. B **95**, 075128 (2017).

[35] Y. Niimi, T. Matsui, H. Kambara, K. Tagami, M. Tsukada, and H. Fukuyama, Scanning tunneling microscopy and spectroscopy studies of graphite edges, Appl. Surf. Sci. **241**, 43 (2005).

[36] Y. Kobayashi, K.-I. Fukui, T. Enoki, K. Kusakabe, and Y. Kaburagi, Observation of zigzag and armchair edges of graphite using scanning tunneling microscopy and spectroscopy, Phys. Rev. B **71**, 193406 (2005).

[37] K. Sasaki, S. Murakami, and R. Saito, Stabilization mechanism of edge states in graphene, Appl. Phys. Lett. **88**, 113110 (2006).

[38] W. Yao, S. A. Yang, and Q. Niu, Edge states in graphene: From gapped flat-band to gapless chiral modes, Phys. Rev. Lett. **102**, 096801 (2009).

[39] M. Costa, B. Focassio, L. M. Canonico, T. P. Cysne, G. R. Schleder, R. B. Muniz, A. Fazzio, and T. G. Rappoport, Connecting higher-order topology with the orbital Hall effect in monolayers of transition metal dichalcogenides, Phys. Rev. Lett. **130**, 116204 (2023).

[40] Y.-L. Sun, G.-H. Chen, S.-C. Du, Z.-B. Chen, Y.-W. Zhou, and E.-J. Ye, Spin-valley polarized edge states in quasi-one-dimensional asymmetric kagome lattice, Front. Phys. **10**, 33836 (2022).

[41] D. Jo, D. Go, and H.-W. Lee, Gigantic intrinsic orbital Hall effects in weakly spin-orbit coupled metals, Phys. Rev. B **98**, 214405 (2018).

[42] Y.-G. Choi, D. Jo, K.-H. Ko, D. Go, K.-H. Kim, H. G. Park, C. Kim, B.-C. Min, G.-M. Choi, and H.-W. Lee, Observation of the orbital Hall effect in a light metal Ti, Nature (London) **619**, 52 (2023).

[43] T. S. Seifert, D. Go, H. Hayashi, R. Rouzegar, F. Freimuth, K. Ando, Y. Mokrousov, and T. Kampfrath, Time-domain observation of ballistic orbital-angular-momentum currents with giant relaxation length in tungsten, Nat. Nanotechnol. **18**, 1132 (2023).

[44] S. Bhowal and G. Vignale, Orbital Hall effect as an alternative to valley Hall effect in gapped graphene, Phys. Rev. B **103**, 195309 (2021).

[45] T. P. Cysne, M. Costa, L. M. Canonico, M. B. Nardelli, R. B. Muniz, and T. G. Rappoport, Disentangling orbital and valley Hall effects in bilayers of transition metal dichalcogenides, Phys. Rev. Lett. **126**, 056601 (2021).